MNRAS **000**, 1–?? (2015) Preprint 1 June 2016 Compiled using MNRAS LATEX style file v3.0

The Distance and Properties of Hydrogen Clouds in the Leading Arm of the Magellanic System

B.-Q. For[1⋆], L. Staveley-Smith[1], N. M. McClure-Griffiths[2], T. Westmeier[1], K. Bekki[1]
[1] *ICRAR, University of Western Australia, Crawley, WA, 6009, Australia*
[2] *Research School of Astronomy & Astrophysics, Australian National University, Canberra, ACT 2611, Australia*

arXiv:1605.09504v1 [astro-ph.GA] 31 May 2016

Accepted 27 May 2016. Received 7 April 2016

ABSTRACT

We present a high-resolution study of five high-velocity clouds in the Magellanic Leading Arm region. This is a follow-up study of our widefield Parkes survey of the region in order to probe the multiphase structures of the clouds and to give an insight to their origin, evolution and distance. High-resolution data were obtained from the Australia Telescope Compact Array. By combining with single-dish data from the Galactic All-Sky Survey (GASS), we are able to probe compact and diffuse emission simultaneously. We identify resolved and unresolved clumps. Physical parameters were derived for both diffuse structure and compact clumps. The latter are cold with typical velocity linewidths of 5 km s^{-1}. We find a gradient in thermal halo pressure, hydrogen density and H I column density of HVC as a function of Galactic latitude. This is possibly the first observational evidence of varying distance in the Leading Arm region, with the leading part of the Leading Arm (LA II and III) probably being closer to the Galactic disc than the trailing end (LA I).

Key words: radio lines: ISM – ISM: structure – ISM: kinematics and dynamics – ISM: clouds

1 INTRODUCTION

High-velocity clouds (HVCs; Muller et al. 1963) are neutral atomic hydrogen gas clouds distributed across the entire sky as large, homogeneous complexes, and include the Magellanic Stream (Mathewson et al. 1974), as well as numerous compact and isolated clouds. They are characterised by a high radial velocity that is forbidden by a simple Galactic rotation model. To classify HVCs, Wakker (1991) introduced the so-called "deviation velocity", which is defined as the smallest difference between the velocity of the cloud and that of the Galactic disc gas along the line-of-sight, and suggested a deviation velocity of at least 50 km s^{-1} for HVCs.

The origin of HVCs has been under debate for decades. A hypothesis of an extragalactic origin was put forward by Blitz et al. (1999). They argued that the observed properties of HVCs are consistent with a distribution across the entire Local Group. In fact, numerical simulations by Klypin et al. (1999) and Moore et al. (1999) suggested that HVCs, excluding some of the large HVC complexes and the Magellanic Stream (MS), might even be the missing dark matter satellites as predicted by cosmological dark matter models. Braun & Burton (1999) conducted a study using the Leiden/Dwingeloo Survey of Galactic neutral hydrogen (LDS; Hartmann & Burton 1997). They identified a subclass of HVCs, namely compact high-velocity clouds (CHVCs), which are isolated, have an angular diameter of $\leqslant 2^\circ$ and H I column densities above 1.5×10^{18} cm^{-2}. These CHVCs were again claimed to be at extragalactic distance. However, surveys of local galaxy groups showed no detection of similar H I clouds (Zwaan 2001; Pisano et al. 2004). A more detailed study of a subsample of CHVCs concluded that they are most likely circumgalactic objects with distances of the order of 100 kpc (Westmeier et al. 2005).

Many CHVCs have a head-tail morphology (Brüns et al. 2000; Putman et al. 2011), suggesting that gas has been stripped via ram-pressure interaction with the ambient medium. A recent simulations of Salem et al. (2015) has shown such ram-pressure effect on the Large Magellanic Cloud (LMC). Some of the head-tail clouds have been studied in detail, such as HVC 125+41-207 (Brüns et al. 2001), HVC 289+33+251 (Brüns & Westmeier 2004), HVC 291+26+195 and HVC 297+09+253 (Ben Bekhti et al. 2006, hereafter BBKW06). In many cases, they reveal two-component line profiles consisting of a cold core surrounded by a warm envelope. Nevertheless, numerical studies are somewhat

⋆ E-mail:biqing.for@icrar.org

© 2015 The Authors

inconclusive about the existence of two-phase structures in HVCs with z greater than $\sim$ 20 kpc in a $T \sim 10^6$ K halo (Wolfire et al. 1995). Observationally, two-phase HVCs have been found in the Magellanic Stream and Leading Arm (LA) (e.g. see Stanimirović et al. 2008; For et al. 2013, 2014), which have estimated distances between 20 and 100 kpc. This implies that the thermal pressure and halo density beyond 10 kpc is not well understood.

In this paper, we study the multiphase structure of a subsample of HVCs in the region of the LA (For et al. 2013, hereafter FSM13). The aims are (1) to resolve any multiphase structure, (2) derive physical parameters, (3) study physical properties, in particular the thermal pressure in different regions to probe environmental effects. The paper is organised as follows: in §2, we list the selection criteria for the targets. §3 gives a decription of our observational setup, data acquisition and reduction process. §4 describes the analysis methodology. Our results and interpretation are presented in §5. We compare the results with previous studies and discuss the implications for the Galactic halo by comparing our results with a model in §6 and §7. Finally, a summary is given in §8.

2 TARGET SELECTION

We selected five HVCs from the FSM13 catalog. The selection criteria are based on the following: (a) the peak brightness temperature of the HVC is $\sim 10\sigma$ above the brightness temperature sensitivity for the instrument setup and array configuration (see §3); (b) the HVC has a velocity linewidth of less than 10 km s^{-1}; (c) the HVC has a distinct morphological type of head-tail, bow-shock or symmetric as described in FSM13; (d) the HVCs are over a range of different Galactic latitudes. Figure 1 shows the integrated H I column density map of the LA region studied by FSM13, and the observed targets are marked with red circles.

3 OBSERVATIONS AND DATA

Both single-dish and interferometer data are used for this study. While single-dish data probe the diffuse emission, the interferometer data allow us to probe small-scale structures. We employed data from the second data release of the single-dish Parkes Galactic All-Sky Survey (GASS; McClure-Griffiths et al. 2009) in this study. This has been corrected for stray radiation and radio frequency interference (Kalberla et al. 2010). GASS is an HI survey of the entire sky south of declination +1° using the 20-cm multibeam receiver on the Parkes radio telescope. GASS covers $V_{\rm LSR}$ between −400 and +500 km s^{-1}. The data have a channel width of 0.82 km s^{-1}, a spectral resolution of 1 km s^{-1}, a brightness temperature (T_B) rms sensitivity of 57 mK, and an angular resolution of 16′. We refer the reader to detailed descriptions of GASS and data processing in McClure-Griffiths et al. (2009) and Kalberla et al. (2010).

The high-resolution H I observations were carried out at the Australia Telescope Compact Array (ATCA) in Narrabri using the EW367 and EW352 configurations in November 2012 and January 2013, respectively. Only five out of the six antennas were used for the analysis. The inner five antennas of the EW367 configuration cover baselines between 92 m and 367 m. The EW352 configuration covers baselines between 31 m and 352 m. We used the zoom mode option of the Compact Array Broadband Backend (CABB; Wilson et al. 2011) for the observations, which has a total bandwidth of 2 GHz with 1 MHz (coarse) and 0.5 kHz (fine) resolutions. We centered the zoom band on 1420 MHz. This configuration results in a velocity resolution of 0.1 km s^{-1}.

We observed the primary flux calibrator PKS 1934-638 at the beginning of each observing session. A secondary phase calibrator, which is located nearby the target field, was observed for 3 min every hour. Each observing session was about 10–12 h long, so achieved good uv-coverage. We also adopted the strategy of obseving two targets per observing session by alternating between them. The beam was centered on the coordinates listed in the FSM13 catalog.

The data reduction was performed in a standard manner using MIRIAD (Sault et al. 1995). To create dirty images, we adopted robust weighting of 0 for four of the HVCs, which optimizes resolution and sensitivity. For HVC 310+08+167, a robustness parameter of 2 was used in order to match for its low surface brightness. A small selected region with H I emission in each dirty cube was deconvolved using the Steer CLEAN algorithm (Steer et al. 1984). The final data cubes were corrected for primary beam attenuation and have an rms noise of about 10 mJy per beam.

To circumvent the short-spacing problem of the interferometer data, we combined the ATCA data with the single-dish data from GASS. We adopted the linear method, merging in the Fourier domain (Stanimirović 2002). With this method, the GASS data were converted to Jy per beam with a conversion factor of 0.658, regridded spatially and in velocity to match the ATCA image, and then the residual primary beam attenuation present in the ATCA data was applied to the GASS data prior to combining them. We smoothed the combined data cube spatially using the CONVOL task. The cubes are smoothed to full width half maxima (FWHM) of 150″, 150″, 160″, 200″ and 300″ for HVC 252.2−20.5+310, HVC 266.0−18.7+338-18, HVC 276.3−09.0+277, HVC 297.1+08.5+253, HVC 310.3+08.1+167, respectively. We also smoothed the cubes spectrally over 3 channels using a Hanning function and extracted the channels that contain H I emission. As the sensitivity drops off quickly toward the outer edge of the beam, we used the ATCA primary beam model to mask out the noise at the outer edge of the data cube. Then, we created the integrated H I column density maps of 5 clouds as shown in Figure 2.

4 ANALYSIS

We analyze the GASS and the combined ATCA and GASS data separately for each cloud. For the GASS data, spectra are extracted along the symmetry axis of each cloud to derive the physical parameters of peak H I column density ($N_{\rm HI}$), velocity in the Local Standard of Rest frame ($V_{\rm LSR}$) and velocity linewidth (Δv). In Figures 3–7, we show the extracted spectra (left), integrated H I column density map (top right) and the derived physical parameters along the symmetry axis (bottom right) for each cloud. The

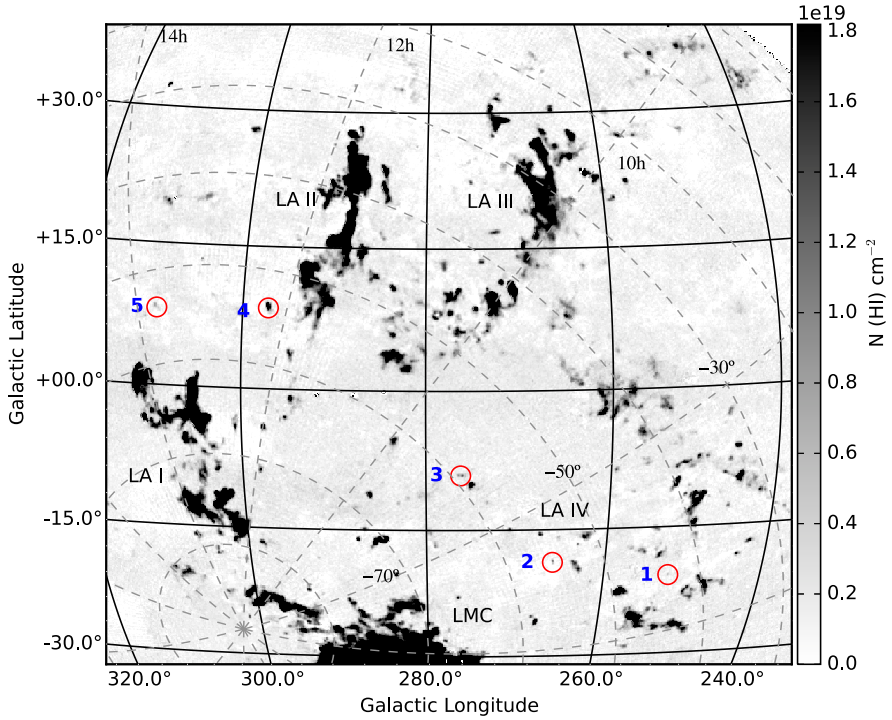

Figure 1. Integrated H I column density map in the region of the LA as studied by FSM13. The red circles mark the clouds selected for our ATCA observations at different Galactic latitudes. Equatorial coordinates are overlaid onto the plot in dashed grey. The labels 1–5 correspond to HVC 252.2-20.5+310, HVC 266.0-18.7+338, HVC 276.3-09.0+277, HVC 297.1+08.5+253 and HVC 310.3+08.1+167, respectively. Three of the clouds are part of the LA IV.

white crosses in the integrated H I column density map represent the positions of individual spectra along the sliced axis. The series of extracted spectra are fitted with either a single or double Gaussian profile, in which amplitude, velocity center and variance are set as free parameters. Examples of double Gaussian fits are shown in Figure 8. We calculate the integrated H I column density using $N_{\rm HI} = 1.823 \times 10^{18} \int T_{\rm B} dv = 1.823 \times 10^{18} \cdot T_{\rm B} \cdot \sigma\sqrt{2\pi}$, where $T_{\rm B}$ is peak brightness temperature in K, v is the velocity in km s^{-1}, and σ is the standard deviation in km s^{-1}. The velocity linewidth is calculated using the derived σ, $\Delta v = \sigma\sqrt{8\ln(2)}$. The derived results are shown in the bottom right panel of Figures 3–7, with red crosses indicating the narrow linewidth component of the cloud. The derived physical parameters using GASS data are summarized in Table 1.

For the combined data, we run a 3-dimensional version of CLUMPFIND, which is an automatic routine for analyzing clumpy structure in spectral line data cubes (Williams et al. 1994). The routine searches the local peaks of the emission and follows them down to the user defined intensity level. We note that CLUMPFIND has its limitations if the data cube contains significant background noise. After running CLUMPFIND, we inspect the output manually to eliminate false detections. Identified clumps in each cloud are shown in Figure 9 with crosses and labels. We perform a similar analysis as for the GASS data by extracting the spectra of the clumps at peak H I column density and deriving their physical parameters. A summary of the derived physical parameters of these clumps is given in Table 2.

5 OVERALL PROPERTIES OF THE HVCS

Four of the HVCs studied here are classified as head-tail clouds. The only exception, HVC 266.0−18.7+338, is classified as a symmetric cloud by FSM13. However, the outer diffuse envelope makes the classification ambigious. It may also be a head-tail cloud.

The head-tail morphology suggests ram-pressure interaction with the ambient medium. FSM13 reveal multiphase structures, which resemble broad and narrow components. We consider the broad component to be >10 km s^{-1} in this study. On average, the velocity linewidths for the broad and narrow component are 20 km s^{-1} and 6.2 km s^{-1}, respectively. Most of the identified clumps only have a cold core. There are also unresolved clumps showing multiphase structures with broad and cold components or cold components only.

Table 1. Derived physical parameters of each cloud either using a single or double Gaussian profile. GASS data are used and the position number represents the location of extracted spectrum.

Name	Position #	T_{B_1} (K)	T_{B_2} (K)	V_{LSR_1} (km s^{-1})	V_{LSR_2} (km s^{-1})	N_{HI_1} (10^{18}cm^{-2})	N_{HI_2} (10^{18}cm^{-2})	Δv_1 (km s^{-1})	Δv_2 (km s^{-1})
HVC 252.2-20.5+310	1	...	0.06	...	306.1	...	3.30	...	30.7
	2	...	0.10	...	308.1	...	4.09	...	22.1
	3	...	0.18	...	310.1	...	5.71	...	16.5
	4	0.22	0.11	311.1	308.7	4.07	6.70	9.7	30.4
	5	0.29	0.14	310.8	309.8	5.38	7.24	9.4	26.5
	6	0.26	0.23	310.2	309.9	3.19	9.55	6.4	21.2
	7	0.18	0.23	310.6	309.2	1.67	6.98	4.8	15.6
	8	0.20	0.13	311.1	308.2	2.07	4.77	5.4	19.0
	9	0.14	0.10	310.4	305.3	2.34	6.57	8.5	35.5
	10	0.08	0.08	309.9	309.7	1.29	4.81	7.9	32.1
	11	0.07	0.07	310.7	309.6	0.63	3.87	4.7	28.3
	12	...	0.08	...	307.8	...	4.08	...	24.9
HVC 266.0-18.7+338	1	0.20	...	340.5	...	3.61	...	9.4	...
	2	0.20	0.21	339.6	341.5	1.63	4.71	4.2	11.3
	3	0.30	0.30	339.8	340.5	2.48	7.13	4.3	12.2
	4	0.46	0.26	339.8	339.0	4.68	8.94	5.3	18.0
	5	0.48	0.27	339.1	337.6	6.22	11.21	6.7	21.3
	6	0.49	0.22	338.1	335.5	8.56	12.09	9.1	27.8
	7	0.35	0.24	336.9	334.7	6.11	12.49	9.0	27.3
	8	0.24	0.29	336.2	334.0	2.24	12.71	4.9	23.0
	9	0.18	0.23	336.1	333.4	1.34	9.51	3.9	21.3
	10	0.13	0.13	335.6	332.8	1.35	6.06	5.5	23.7
	11	...	0.13	...	333.7	...	4.68	...	18.3
HVC 276.03-09.0+277	1	...	0.16	...	277.6	...	4.64	...	14.6
	2	0.18	0.20	280.0	277.4	2.21	6.84	6.5	17.4
	3	0.37	0.09	279.5	272.4	7.10	2.80	10.0	16.2
	4	0.27	...	278.0	...	5.20	...	9.9	...
	5	0.45	0.07	277.2	273.4	6.27	2.59	7.1	19.6
	6	0.65	0.20	277.2	274.9	8.26	7.12	6.5	18.2
	7	0.65	0.10	277.1	274.4	8.80	4.13	7.0	21.3
	8	0.30	...	276.8	...	4.52	...	7.7	...
HVC 297.1+08.5+253	1	...	0.17	...	249.7	...	7.31	...	22.1
	2	...	0.30	...	251.1	...	13.30	...	23.0
	3	...	0.44	...	253.1	...	19.92	...	23.4
	4	...	0.47	...	253.8	...	20.05	...	21.8
	5	...	0.57	...	254.0	...	24.23	...	22.0
	6	...	0.64	...	253.3	...	26.46	...	21.4
	7	0.21	0.70	252.9	252.5	2.55	29.74	6.1	22.0
	8	0.46	0.76	252.7	252.9	3.81	31.90	4.3	21.6
	9	1.15	0.67	252.6	252.9	8.69	20.31	3.9	15.5
	10	1.82	0.69	252.6	253.1	14.52	26.57	4.1	19.7
	11	1.99	0.54	252.6	252.9	15.28	17.92	4.0	17.3
	12	2.02	0.38	252.6	252.7	12.92	13.54	3.3	18.4
	13	1.03	0.22	252.5	252.5	6.45	5.87	3.2	13.6
	14	0.35	0.27	252.0	252.9	1.62	3.05	2.4	5.8
HVC 310.3+08.1+167	1	0.07	0.08	161.3	160.0	0.46	1.99	3.4	13.2
	2	...	0.14	...	160.7	...	3.39	...	12.2
	3	...	0.17	...	161.1	...	6.93	...	21.3
	4	0.06	0.12	160.1	163.6	0.86	4.95	7.0	21.3
	5	...	0.15	...	163.7	...	4.07	...	14.4
	6	...	0.16	...	165.0	...	4.56	...	14.5
	7	0.11	0.14	164.7	166.5	1.77	4.97	8.6	18.2
	8	0.10	0.12	166.7	165.9	0.79	4.41	4.0	18.4
	9	...	0.20	...	166.6	...	4.98	...	13.1
	10	...	0.36	...	168.3	...	7.05	...	10.1
	11	0.17	0.42	168.9	168.1	0.67	7.63	2.1	9.4
	12	0.42	0.06	167.9	161.0	5.69	3.16	7.0	25.3
	13	0.20	0.08	168.3	164.0	2.36	2.38	6.1	15.3

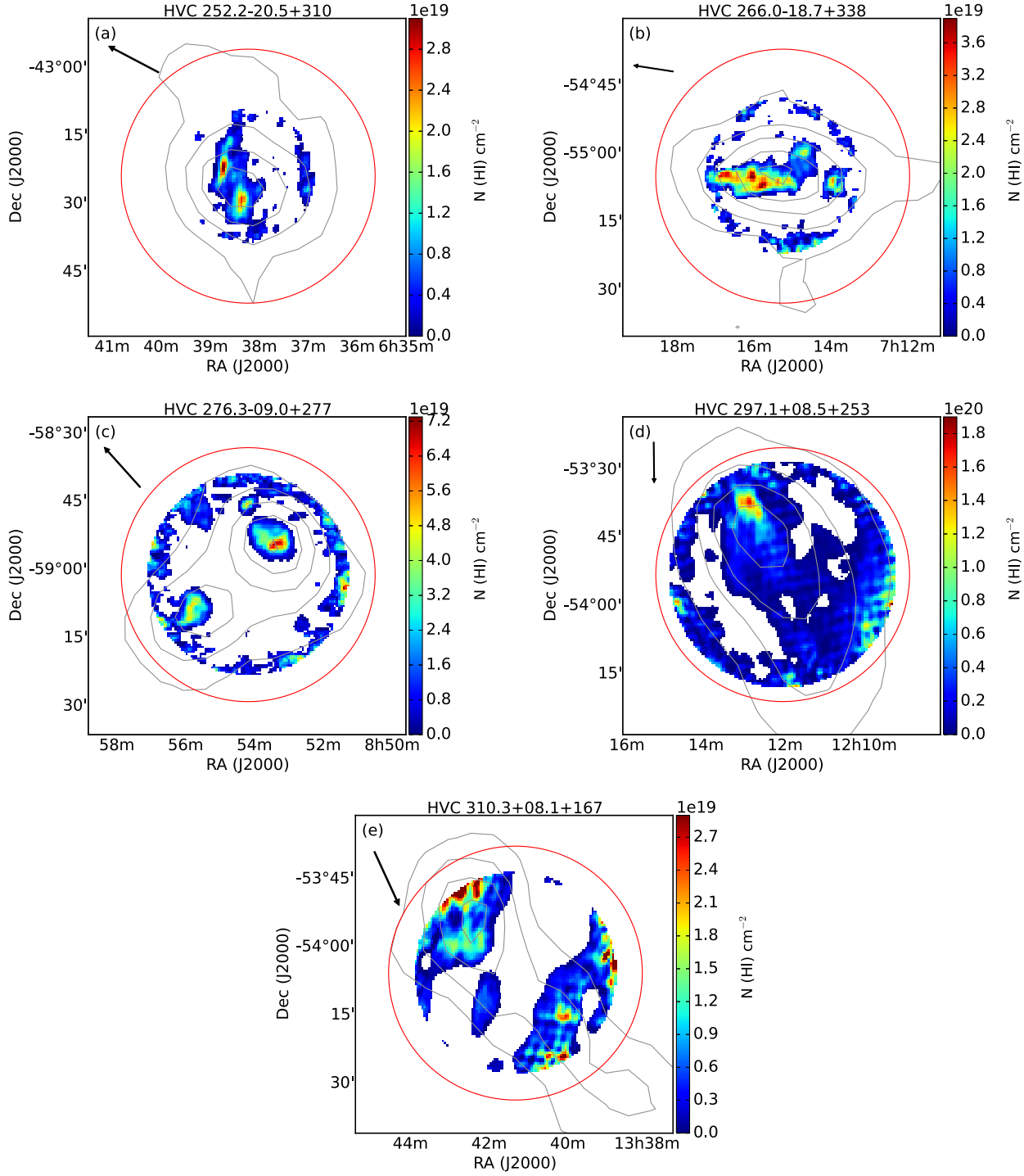

Figure 2. Integrated H I column density maps of the combined Parkes and ATCA H I data set. The red circles indicate the 12 percent of peak sensitivity area of the image. The analyzed regions as shown here are based on the percentage of the peak sensitivity. The grey contours represent H I column densities in the GASS data set. The arrows point in the direction of the Galactic plane.

5.1 HVC 252.2−20.5+310

HVC 252.2-20.5+310 is part of the LA IV. The tail is pointing away from the Galactic Plane. In Figure 3, we show the spectral line profiles and derived physical parameters along the sliced axis of the cloud. The cloud is sliced from south to north with a designated position number. Multiphase structures of warm (broad) and cold (narrow) components at the head of the cloud are seen in the series of spectral line profiles. The rise and fall of the H I column density is gradual. There is no obvious velocity gradient across this cloud. We find that the cold component (red crosses) has a fairly consistent $V_{\rm LSR} \sim 311$ km s^{-1}. The FWHM of the warm com-

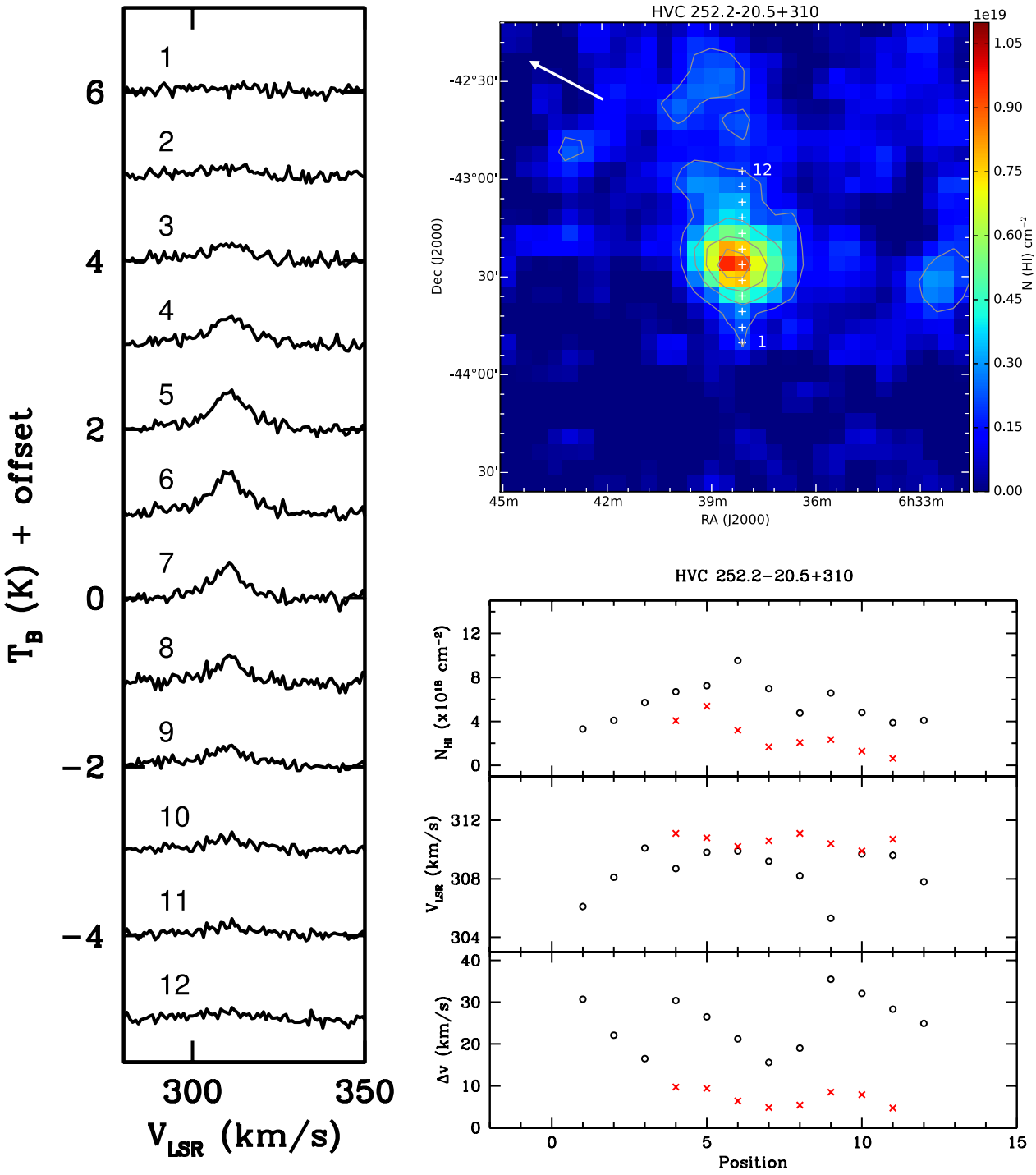

Figure 3. Top right: Integrated H I column density map of HVC 252.2-20.5+310 in the GASS data set. The contour levels correspond to H I column densities ($N_{\rm HI}$) of 0.2, 0.4, 0.6, 0.8, 1.0×10^{19} cm^{-2}. The white crosses represent the positions along the sliced axis of the cloud. It is sliced from south to north with a designated position number. The arrow points in the direction of the Galactic plane. **Left:** Series of extracted spectra along the sliced axis. **Bottom right:** Physical parameters of the cloud as derived from the spectra. Black circles and red crosses represent the broad and narrow component, respectively.

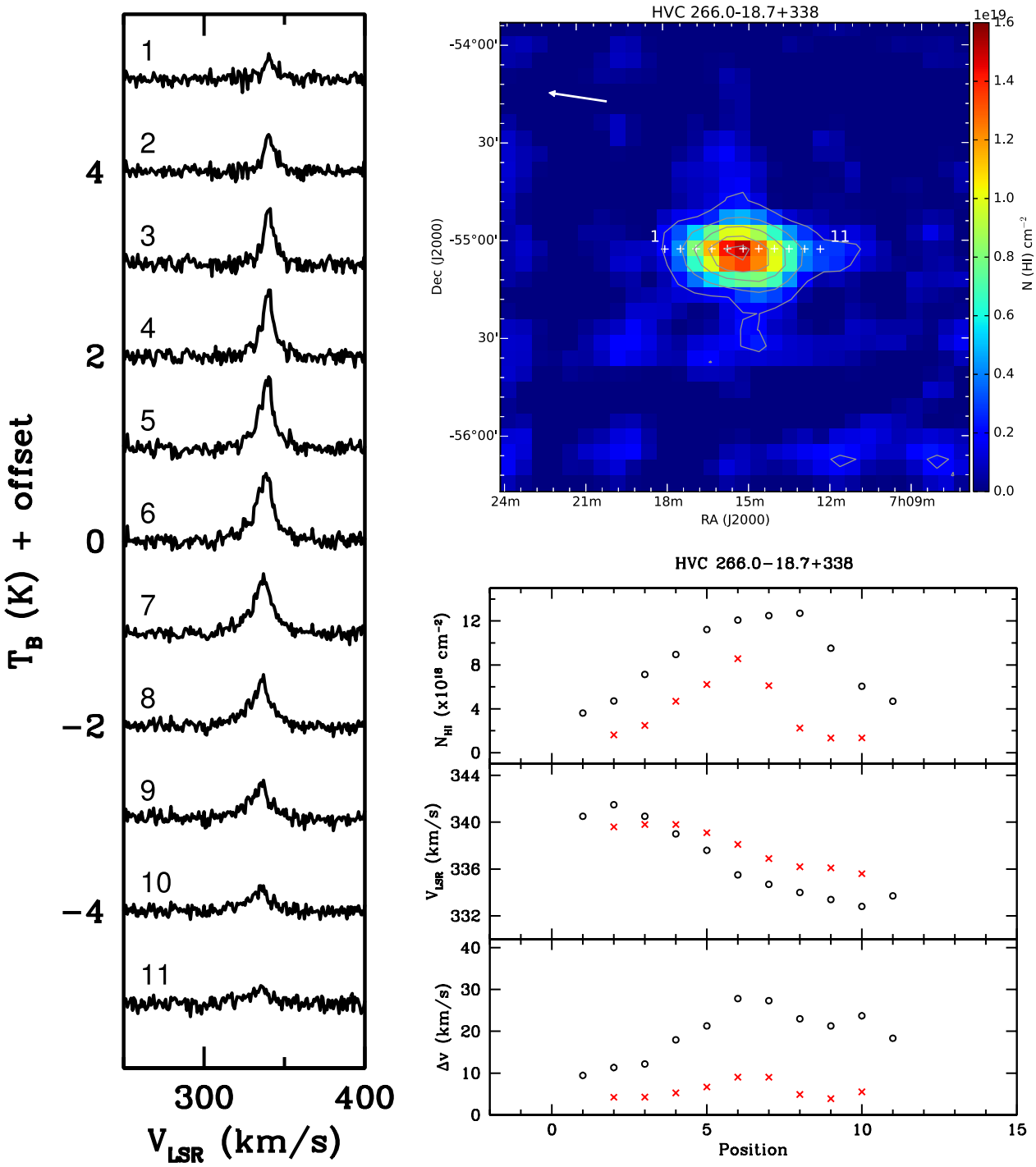

Figure 4. Same as Figure 3 except for HVC 266.0-18.7+338. The contour levels correspond to 0.2, 0.5 , 0.8, 1.1, 1.40×10^{19} cm^{-2} and the cloud is sliced from east to west.

ponent (black circles) varies in different parts of the cloud. The cold component has a typical linewidth of 7 km s^{-1}.

Figure 2a shows the peak H I column density map of the combined image. The overlaid contour provides the spatial size of the cloud as observed by GASS. As seen in the figure, the head of the cloud has been resolved into two clumps. The morphology of these two clumps is outlined with contours in Figure 9a. Clumps A and B morphologically look like head-tail clouds which are pointing in the opposite direction. The derived physical parameters at the peak H I column density of both clumps are presented in Table 2. Clump A has two unresolved components, which have Δv of 2.80 and

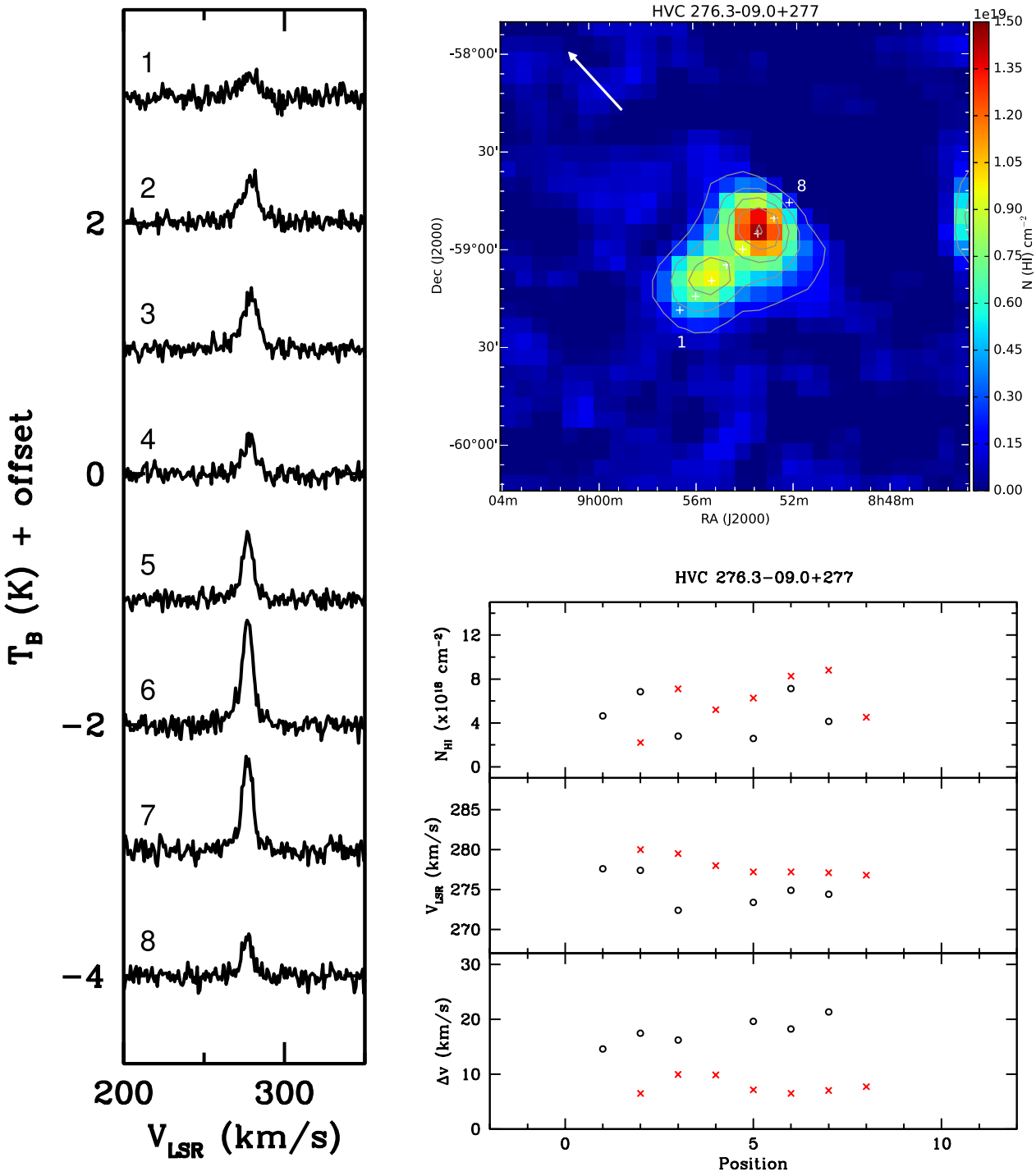

Figure 5. Same as Figure 3 except for HVC 276.3-09.0+277. The contour levels correspond to 0.2, 0.5 , 0.8, 1.1, 1.40×10^{19} cm^{-2} and the cloud is sliced from south-east to north-west.

7.38 km s^{-1}. Clump B is resolved with a single peak T_B of 2.78 K.

5.2 HVC 266.0−18.7+338

HVC 266.0-18.7+338 is also part of the LA IV. It is classified as a symmetric cloud in FSM13. The cloud is sliced from east to west, which corresponds to the spectral line profiles from top to bottom in Figure 4. The cloud shows a clear velocity gradient with velocity decreasing from about 340 km s^{-1} to

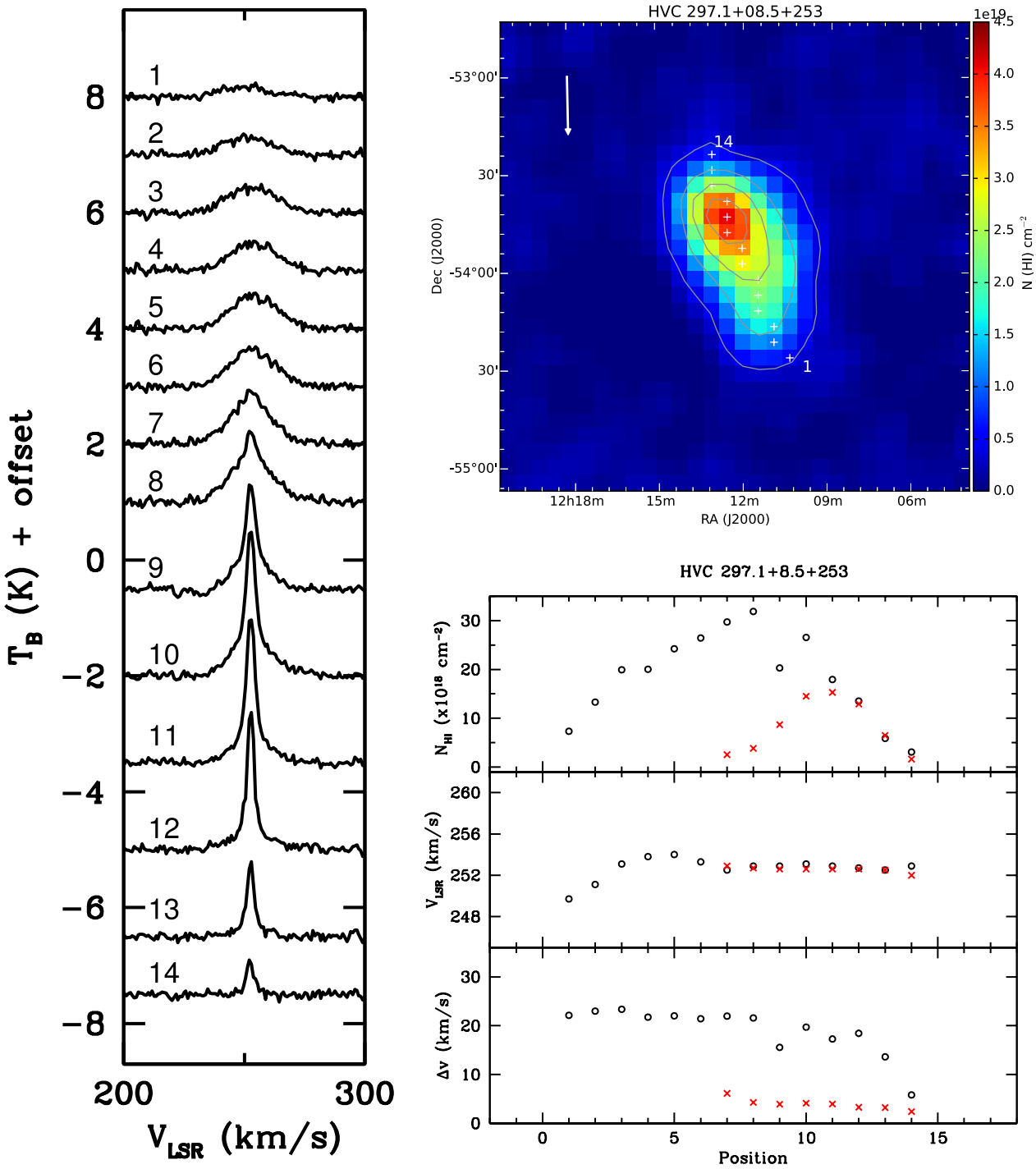

Figure 6. Same as Figure 3 except for HVC 297.1+08.5+253. The contour levels correspond to 0.5, 1.5, 2.5, 3.5, 4.5×10^{19} cm^{-2} and the cloud is sliced from south-west to north-east.

332 km s^{-1}. In general, the cold component has a velocity larger than the warm component. The effect can be seen in the series of asymmetric spectral line profiles. The Δv of the warm component increases from the east end of the cloud and reaches a maximum at the center before flattening it out to $\sim$ 25 km s^{-1}. A similar trend is seen in Δv of the cold component. The linewidth and velocity gradients indicate that this cloud is probably a head-tail cloud rather than a symmetric cloud.

The ATCA primary beam almost covers the entire cloud (see Figure 2b). The combined image reveals a complex structure. Figure 9 shows a total of 5 distinct clumps identi-

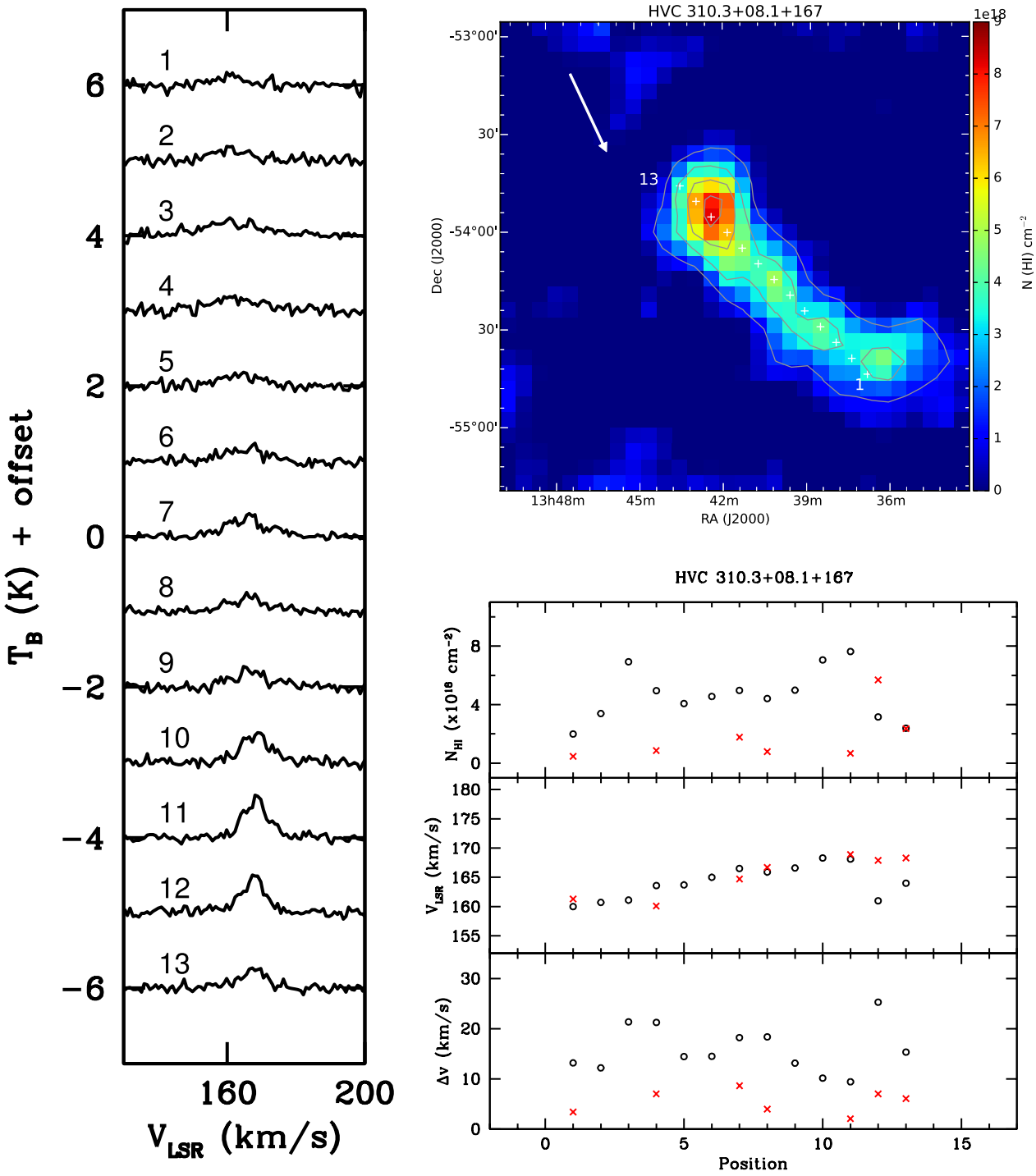

Figure 7. Same as Figure 3 except for HVC 310.3+08.1+167. The contour levels correspond to 1.5, 3.5, 5.5, 7.5, 9.5×10^{18} cm^{-2} and the cloud is sliced from south-west to north-east.

fied via CLUMPFIND, named A–E. All clumps are resolved. These clumps have a fairly similar $V_{\rm LSR}$ (336–341 km s^{-1}). Clump D and E are considered warm with $\Delta v > 10$ km s^{-1}. Both of them are also isolated from the main concentration of other clumps. None of them has a distinct morphology.

5.3 HVC 276.3−09.0+277

HVC 276.3-09.1+277 is the third HVC in this study that is located in LA IV. This head-tail cloud has two main cores with one being at the head of the cloud and the other at the tail (see Figure 5). The analysis is performed by slicing the cloud diagonally from south-east to north-west. The cloud

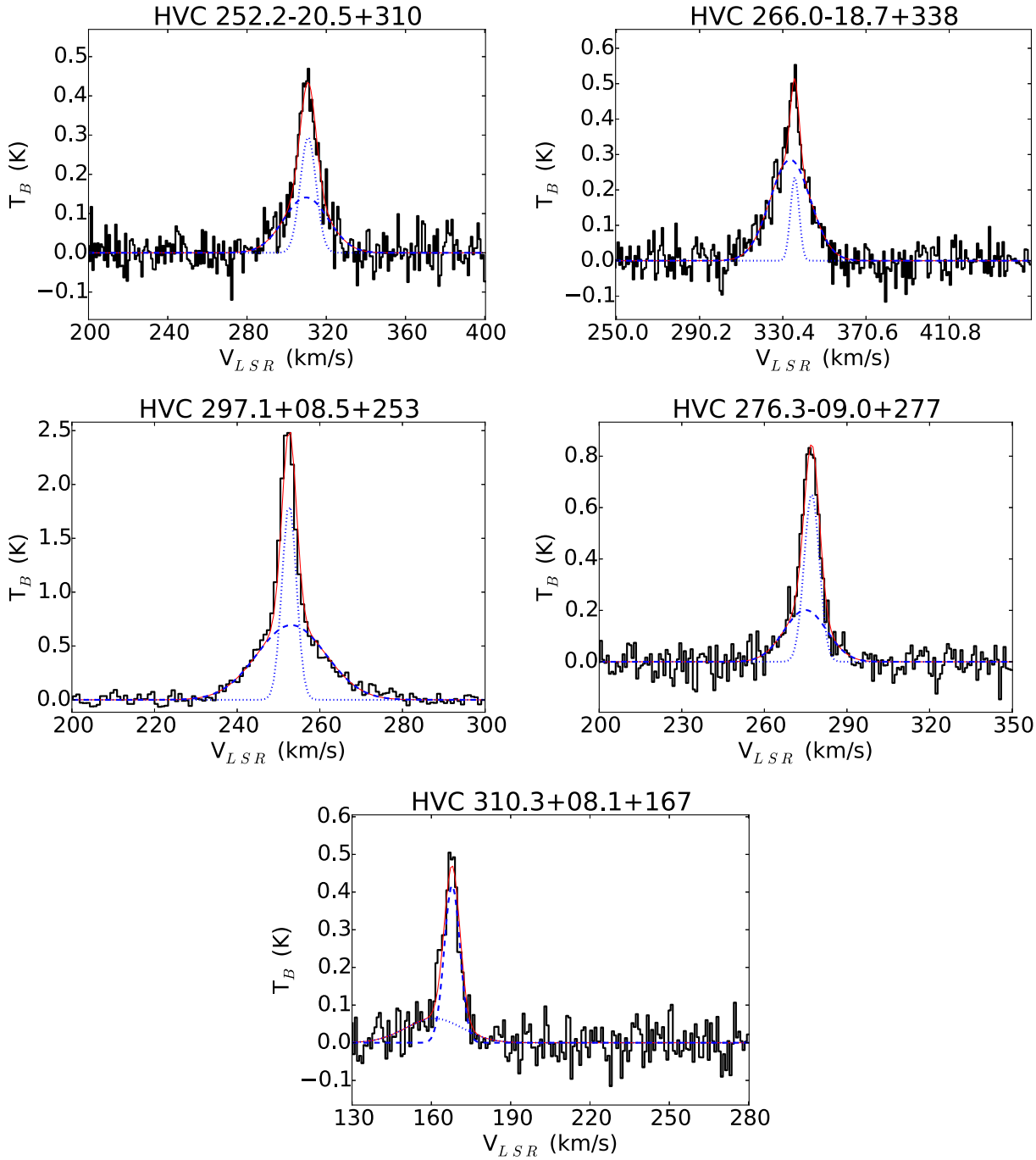

Figure 8. Examples of double Gaussian fits to a spectrum from each cloud. Red indicates the combined profile of the two Gaussian profiles.

does not show a clear velocity gradient. Its head is rather compressed. The average Δv for all of the cold components is 7.5 km s^{-1}. The $V_{\rm LSR}$ values of the cold components decrease gradually and are larger than the warm components. The peak $T_{\rm B}$ is $\sim$0.7 K at the main core of the cloud.

In Figures 2c and 9c, we show the resolved clumps in the combined image. Three clumps are identified. Clump A is located in the main core of the cloud but clump B is displaced slightly from the second core of the cloud as seen in the diffuse emission. Both clump A and B are morphologically similar to head-tail clouds. Clump C is relatively smaller than clump A and B. It is unresolved and consists of two cold components, which have Δv of 3.25 and 9.44 km s^{-1}.

5.4 HVC 297.1+08.5+253

HVC 297.1+08.5+253 is situated in the vicinity between LA I and II, closer to the south-eastern part of LA II. This head-tail cloud is morphologically slightly different from HVC 252.2−20.5+210. The contours show a typical head-tail

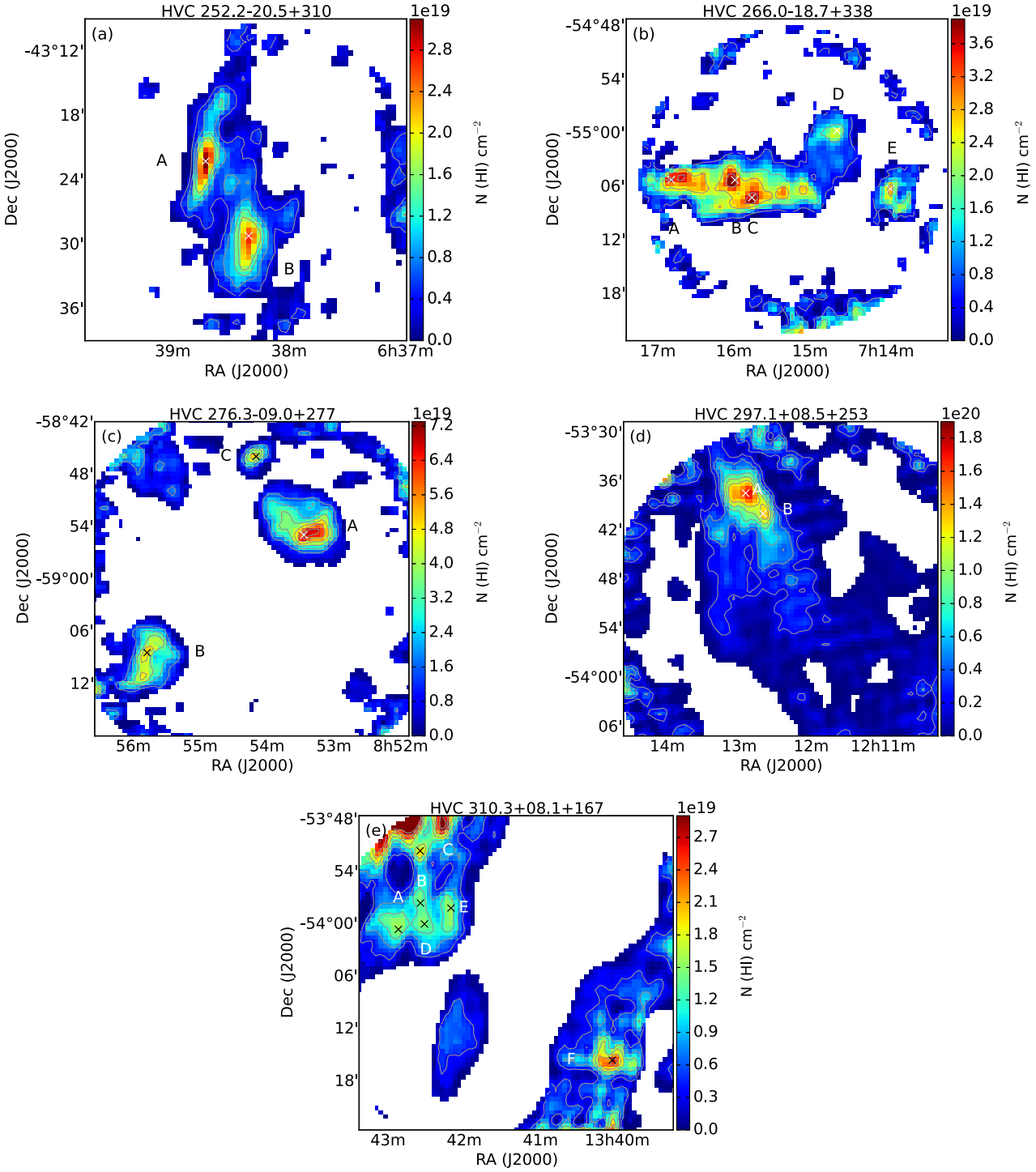

Figure 9. Integrated H I column density maps of the combined Parkes and ATCA H I data sets. Identified clumps are marked with a cross and are labeled. Contours are plotted to highlight the morphology of the clumps.

structure (see Figure 6). The tail of HVC 297.1+08.5+253 is pointing away from the Galactic plane.

In Figure 6, the spectral line profiles (top to bottom) represent the sliced positions of the cloud from south-west to north-east. As expected, the peak H I column density increases toward the head of the cloud. Interestingly, the derived H I column density of the warm component reaches its maximum (position 8) before the maximum H I column densities as shown in the GASS integrated H I column density map at positions 9 and 10. The cold component also shows the same rise and fall pattern in H I column density but with the maximum at position 11. The $V_{\rm LSR}$ shows a small gradient at the tail of the cloud and then becomes constant at 253 km s^{-1} for both cold and warm component. Half of

Table 2: Derived physical parameters and location of each clump found in the combined data.

Name	Clump	RA	Dec	T_{B_1} (K)	T_{B_2} (K)	V_{LSR_1} (km s^{-1})	V_{LSR_2} (km s^{-1})	N_{HI_1} (10^{19} cm^{-2})	N_{HI_2} (10^{19} cm^{-2})	Δv_1 (km s^{-1})	Δv_2 (km s^{-1})	T_k (K)	θ (°)	n^b (cm^{-3})	P/k_B^b (K cm^{-3})
HVC 252.2-20.5+310	A	$06^h38^m42.26^s$	$-43°22'14.43''$	3.49	1.27	312.5	313.4	1.89	1.82	2.80	7.38	...	...	...	...
	B	$06^h38^m20.27^s$	$-43°29'14.73''$	2.78	...	310.8	...	2.50	...	4.65	...	471.37	0.144	0.13	60.78
HVC 266.0-18.7+338	A	$07^h16^m36.77^s$	$-55°05'14.92''$	3.29	...	340.9	...	4.04	...	6.33	...	872.96	0.052	0.58	503.19
	B	$07^h16^m01.82^s$	$-55°05'16.69''$	3.78	...	341.3	...	4.34	...	5.92	...	764.99	0.040	0.80	610.84
	C	$07^h15^m44.38^s$	$-55°07'17.20''$	3.52	...	339.5	...	4.37	...	6.40	...	893.88	0.048	0.68	604.95
	D	$07^h14^m38.03^s$	$-54°59'46.95''$	1.24	...	338.2	...	2.51	...	10.41	...	2361.77	0.056	0.33	779.77
	E	$07^h13^m55.98^s$	$-55°06'15.34''$	2.07	...	336.0	...	5.28	...	13.16	...	3772.62	0.049	0.80	3017.05
HVC 276.03-09.0+277	A	$08^h53^m26.09^s$	$-58°54'57.38''$	6.67	...	276.5	...	7.95	...	6.14	...	823.07	0.056	1.05	864.63
	B	$08^h55^m46.20^s$	$-59°08'54.81''$	3.69	...	281.0	...	4.70	...	6.56	...	937.18	0.042	0.83	781.87
	C	$08^h54^m08.70^s$	$-58°45'56.93''$	2.39	5.99	273.5	275.5	4.39	3.78	9.44	3.25	...	...	...	...
HVC 297.1+08.5+253	A	$12^h12^m51.88^s$	$-53°37'28.63''$	20.29	4.38	252.8	249.5	12.99	1.88	3.30	2.21	...	...	...	...
	B	$12^h12^m38.40^s$	$-53°39'29.49''$	11.69	...	252.9	...	11.13	...	4.91	...	524.91	0.028	3.00	1572.20
HVC 310.3+08.1+167[a]	A	$13^h42^m50.09^s$	$-54°00'33.46''$	0.72	0.23	165.5	172.3	0.70	0.15	5.02	3.31	...	...	...	...
	B	$13^h42^m32.98^s$	$-53°57'34.32''$	0.30	0.61	172.2	166.2	0.21	0.70	3.56	5.94	...	...	...	...
	C	$13^h42^m32.80^s$	$-53°51'33.45''$	0.29	0.57	163.5	169.5	0.26	0.59	4.69	5.34	...	...	...	...
	D	$13^h42^m29.65^s$	$-54°00'04.75''$	0.29	0.55	172.5	166.6	0.20	0.63	3.42	5.86	...	...	...	...
	E	$13^h42^m09.20^s$	$-53°58'05.56''$	0.32	0.12	171.9	167.1	0.28	0.11	4.56	4.63	...	...	...	...
	F	$13^h40^m02.87^s$	$-54°15'34.20''$	0.28	0.16	167.4	161.6	0.31	0.17	5.57	5.47	...	...	...	...

a: Parameters are derived from a spatially and spectrally smoothed data cube.
b: Assuming a distance of 25 kpc.

the cloud consists of warm component only, with an average velocity linewidth of 20.1 km s^{-1}. At position 14, two components are detected (refer bottom panel of Figure 6). These two components on avarage have a velocity linewidth of 4.1 km s^{-1}.

The cloud is relatively diffuse as shown in the combined image (Figure 2d). The main resolved feature is offset and leading the diffuse core of the cloud as seen in the GASS image. This explains why the H I column density of the cold component peaks at position 11 in the analysis of the GASS image. Figure 9d shows the resolved feature and two detected clumps. Unfortunately, the feature is detected fairly close to the edge of the ATCA beam, where sensitivity drops off significantly. Thus, extended features cannot be seen.

Clump A has the highest T_B (∼20.3 K) amongst the detected clumps in this study. Clump A is resolved and reveals sub-components as seen in its spectral line profile (not shown here). The resolved clump B has Δv of ∼ 5 km s^{-1}.

5.5 HVC 310.3+08.1+167

HVC 310.3+08.1+167 is located north of LA I. It is pointing in the general direction of motion of LA I. This cloud is quite diffuse compared to the other clouds in this study, It has a very long diffuse tail, which spans nearly 1.5°, and a slight kink at the end (see Figure 7). While this cloud has a lower V_{LSR} than other selected HVCs in this study, it is assumed to be part of the LA based on the constraints listed in FSM13 to exclude the Galactic H I emission.

The analysis is performed by slicing along the symmetry axis from south-west to north-east. The spectral line profiles show that the cloud has a fairly low brightness temperature of ∼0.4 K. The multiple peaks of H I column density indicate numerous components. Apart from the two deviating points at position 12 and 13 in the velocity plot, the gradual increase of V_{LSR} suggests that the cloud has a velocity gradient.

The contours in Figure 2e show that the size of the cloud is a lot larger than the ATCA beam. Since its coordinates were derived at the axis center of the cloud, the core structure was not observed at the center of the ATCA beam, where sensitivity is highest. The low surface brightness nature of the cloud also makes clump idenfication harder. The identification and derivation of physical parameters of the clumps were performed on the smoothed cube. Six distinct clumps have been identified (see Figure 9e). All of them are unresolved and have sub-components. The sub-components are cold as well.

The structure near the head is complex with five clumps being detected within the sensitivity cutoff. They have V_{LSR} ranging from 165 to 172 km s^{-1}. Clump F has a lower V_{LSR} of 161.6 km s^{-1}. They all appear to have an irregular shape.

6 COMPARISON WITH PREVIOUS STUDIES

Two additional compact HVCs, HVC 291+26+195 and HVC 297+09+253, were observed and studied in high-resolution by BBKW06. Both clouds are associated with the LA. BBKW06 analyzed the data obtained from the Parkes H I survey of the Magellanic System (Brüns et al. 2005) and interferometer data observed with the 750D configuration

of the ATCA. By comparing with our integrated H I column density map of the ATCA data alone (not shown here), we find similar resolved structures as seen in Figure 4 of BBKW06. They identified seventeen clumps, which is more than detected in our study, although the method of identification is different. They did not analyze the combined Parkes and ATCA data.

Another high-resolution study of a compact HVC (HVC 289+33+251) has been carried out by Brüns & Westmeier (2004). This cloud is also in the vicinity of LA but a distance of 150 kpc was assumed, which is further than the typical distance of the Magellanic Clouds (50 kpc). This cloud is significantly brighter than our observed targets and has the typical head-tail morphology. It is relatively compact as well. A direct quantitative comparison cannot be achieved due to different resolutions of the two studies.

7 DISCUSSION

7.1 HVC Phase Diagram

HVCs may exist as a stable two-phase medium if the halo pressure lies within a certain range, $P_{\rm min} < P < P_{\rm max}$, where $P_{\rm min}$ and $P_{\rm max}$ are a function of height, z, above the Galactic plane (Wolfire et al. 1995). The phase diagram of thermal pressure, P, vs. hydrogen density, n, can be used to examine the stability of HVCs. To calculate the thermal pressure of the resolved clumps, we apply the ideal gas law, $P/{\rm k} = nT_{\rm k}$, where k is the Boltzmann constant, n is the hydrogen density and $T_{\rm k}$ is the kinetic gas temperature. The upper limit of the kinetic gas temperature can be derived from the velocity linewidth assuming the observed linewidth is dominated by Doppler broadening, $T_{\rm k} = m_{\rm H}\Delta v^2$ / (8 k ln2) = 21.8 $(\Delta v/{\rm km\ s^{-1}})^2$, where $m_{\rm H} = 1.674 \times 10^{-27}$ kg. Assuming spherical symmetry for the clump, $n = N_{\rm HI}$ / (d tanθ), where θ is the angular diameter of the clump and d is the distance to the cloud. The hydrogen density is calculated by assuming distances to the cloud of 25 kpc and 50 kpc. The former distance is close to the kinematic distance derived in McClure-Griffiths et al. (2008). The latter is close to a the measured distance of the LMC (Pietrzyński et al. 2013). Calculated values are presented in Table 2.

Figure 10 shows the phase diagram at different heights z above the Galactic plane overplotted with our derived $P/{\rm k}$ and n for the resolved clumps. Filled and non-filled symbols correspond to the calculated data points by assuming a distance of 25 and 50 kpc, respectively. The inferred z with the assumed distance for each HVC clump is listed next to each symbol. We note that the phase diagram is sensitive to the metallicity (Z) and dust-to-gas ratio (D/G). We adopt the model of $Z = D/G = 0.3$, which is appropriate for stripped LMC gas (Wolfire et al. 1995).

To estimate the effects of uncertainties in our derived P/k and n, we consider various scenarios. Assuming the observed clump is not of spherical shape but an ellipsoid, viewing along the major axis gives a larger angular diameter. Twice the size in angular diameter will result in a decrease in hydrogen gas density by a factor of two. The derived $T_{\rm k}$ is an upper limit given by the velocity linewidth. A decrease of $T_{\rm k}$ by 100 K will result in +0.1 change in log $P/{\rm k}$. Ignoring the two data points near the 50 kpc curve and taking into account the uncertainties, we find that majority of the data points fall onto their corresponding z for the phase diagram. Also, the data points lie in the instability valley of the two-phase medium.

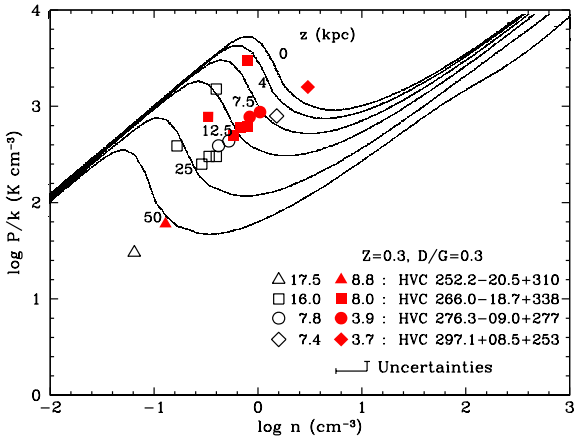

Figure 10. Thermal pressure, $P/{\rm k}$, vs. hydrogen density, n, for various heights, z, above the Galactic plane in kpc. The model of $Z = D/G = 0.3$ is taken from Wolfire et al. (1995). Filled and non-filled symbols represent the calculated data points by assuming a distance of 25 and 50 kpc, respectively. The value next to the symbols in the legend are the calculated heights z, in kpc.

7.2 Halo Environment as a Function of Galactic Latitude

If we assume that the clumps are in hydrostatic equalibrium, the thermal pressure of the clump is equal to the external halo thermal pressure. In Figure 11, we show the average physical parameters of the resolved clumps for each cloud as a function of Galactic latitude. In this case, Galactic latitude is a proxy for z. The height z decreases from negative to positive Galactic latitude. Interestingly, we find a trend of increasing halo thermal pressure, hydrogen density and H I column density with increasing Galactic latitude. This suggests that the clouds reside in a denser halo environment at more positive Galactic latitude. While it has been suggested that the LA is closer to the Galactic centre than the LMC, (McClure-Griffiths et al. 2008), this is the first evidence showing a possible distance gradient in the LA region using compact HVCs that span over $\sim 80^\circ$ in Galactic longitude. The leading part of the LA (LA II and LA III) is most likely closer to our Galaxy than the LA I, which has a kinematic distance of ∼21 kpc (McClure-Griffiths et al. 2008). The study of Venzmer et al. (2012) also showed a similar distance gradient using a different approach. Their investigation was based on the velocity structure of three subpopulations in LA I. Future simulations would be useful to assess the likelihood of such a scenario. We note that $P/{\rm k}$ and n are sensitive to various scenarios as discussed in §7.1. The positive Galactic latitude cloud (HVC 297.14+08.5+253) will have a lower n if it is not spherical but twice the size. The trend of n vs. Galactic latitude becomes less significant in this case.

In FSM13, the formation of the LA IV remains a mystery. It has a very different morphology than its coun-

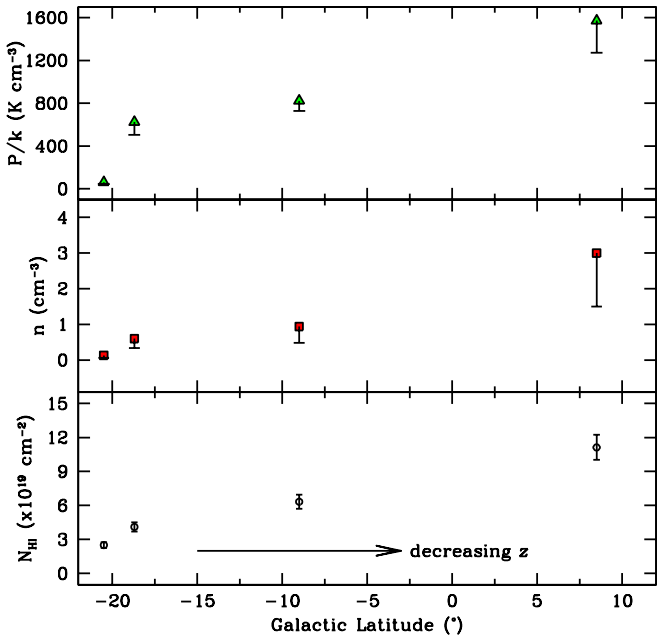

Figure 11. Thermal pressure, P/k, hydrogen density, n, and H I column density, N_{HI}, as a function of Galactic latitude (as a proxy of z). Each data point represents the average physical parameters of all resolved clumps for each cloud. A distance of 25 kpc is assumed here. Uncertainties of P/k and n are discussed in §7.1. A systematic uncertainties of 10% is assumed for N_{HI}. Significantly deviating values, such as the ones for clump D and E of HVC 266.0-18.7+338, are excluded from the calculation. Physical parameters are listed in Table 2.

terpart (LA I–III). This suggests that LA IV might be formed via a different mechanism or has a different origin. The recent discoveries of ultra-faint dwarf galaxies in the vicinity of the Magellanic System (Koposov et al. 2015; Bechtol et al. 2015; Drlica-Wagner et al. 2015) has renewed theoretical and observational interest (see Yozin & Bekki 2015; Westmeier et al. 2015). The model of Yozin & Bekki (2015) confirms that the locations of these ultra-faint dwarf galaxies are associated with the MCs previously as part of a loose group and shows how they are processed by the Galactic halo upon accretion. This suggests that the clumpy LA IV might be the debris from such an accretion event, which might explain why the three HVCs (part of the LA IV) are further away than the two HVCs near LA I and II. This supports the radial distance estimate of 74 kpc for LA IV in Venzmer et al. (2012).

7.3 Star Formation in the Leading Arm Region

Theoretical models and observational evidence show that both the MS and LA were formed via ram-pressure stripping and tidal interaction between the LMC and SMC (see e.g. Diaz & Bekki 2011; For et al. 2013). Both of these mechanisms are known to trigger star formation in galaxies (e.g., galaxy pair NGC 1512/1510, Koribalski & López-Sánchez 2009 and NGC 4522 in the Virgo cluster, Kenney et al. 2004). Star formation in the MS and LA has been postulated but there was no success in the hunt for stars being formed in situ in early years (e.g., Recillas-Cruz 1982; Guhathakurta & Reitzel 1998). Matthews et al. (2009) conducted a search for star formation in the MS regions using cold atomic gas as an indicator. Two absorption components were identified toward a background radio source, J0119−6809. The corresponding H I column density is $\sim 2 \times 10^{20}$ cm^{-1}. Follow up observation shows no detection of CO($J = 1 \rightarrow 0$) molecular gas associated with the cool gas implying that star formation does not occur at that location within the MS.

Neutral hydrogen gas, dust and molecular hydrogen gas (H_2) act as a reservoir for fuelling star formation activities. This is particularly prominent in high gas density regions. Stars are formed when the dense gas clouds reach the Jeans instability and collapse. Measurements of dust and H_2 are fairly limited in the LA region. An attempt for measuring dust, H_2 and metallicity in the LA has been made by Sembach et al. (2001) on a compact HVC (HVC 287.5+22.5+240). They find that the metallicity of this HVC is similar to the SMC, and the detection of H_2 suggests that either the H_2 formed in situ or within the SMC and survived tidal stripping. They prefer the latter scenario given that the formation timescale of H_2 is long ($\sim 10^8$ yr). If the LA is stripped from the SMC as suggested by simulations (e.g., Diaz & Bekki 2011), we would expect the LA region has a similar H_2 and metallicity content as the SMC, and star formation potentially could occur. In fact, a recent attempt to search for stellar components has been carried out at the optical wavelength by Casetti-Dinescu et al. (2014) in the LA region. Five young stars has been successfully identified and they believed to have formed in the LA for the first time, using kinematics information, stellar parameters and distance moduli. We examine the location of these 5 young stars and nearby H I gas content. Four of them are in close proximity of dense clouds with N_{HI} in the range of 1.5×10^{19} to 1.8×10^{20} cm^{-2}. Clouds with these H I column densities exist everywhere in the LA region and yet the search only resulted in five young stars that were born in situ. Where are the missing stars?

The result from §7.1 suggests the possibility of different halo environments in the LA region, which might explain the lack of star formation if a special condition is required to form stars. However, without further information on dust and metallicity properties in the entire LA region, it is very hard to assess the conditions that are needed for star formation to occur. The optical search for young stars is currently limited to specific regions. It would be interesting if future optical studies included candidates located in the vicinity of HVC 287.5+22.5+240 to verify if star formation is plausible with the given conditions.

Metallicity and dust might not be the only factors for the star formation in the region. Observational evidence of interaction between the LA I and Galactic disc gas suggests the gas is being compressed by the Galactic halo gas at low z and star formation could also be triggered.

8 SUMMARY

We have studied five HVCs in the vicinity of the Magellanic Leading Arm. The targets were selected from the FSM13

catalog, and high-resolution observations were carried out at the ATCA. We analyzed the combined single-dish GASS and interferometric ATCA data. Clumps were identified and physical parameters were derived for both clumps and diffuse structure of the HVCs. Most of the clumps have a cold component ($\Delta v < 10$ km s^{-1}). The unresolved clumps generally consist of a warm component only.

Three of the clouds are part of the LA IV, which lies south of the Galactic plane, and have a head-tail like morphology. The other two are located north the Galactic plane and in close proximity to LA I and LA II. HVC 266.0-18.7+338 is the only cloud that shows a clear velocity gradient. It also consists of many clumps. The $V_{\rm LSR}$ of cold clumps is generally larger than the diffuse (warm) component.

In the case of HVC 276.3-09.0+277, its head is compressed and it does not show any velocity gradient. The velocity of the cold component decreases gradually and is larger than that of warm component. Two clumps are located in the two main cores of the cloud. The third clump is relatively small and unresolved. It is located slightly offset from one of the clumps.

HVC 297.1+08.5+253 has been studied by BBKW06. They analyzed the single-dish and interferometer data separately. Their analysis focuses on the core of the head-tail structure and many clumps have been identified. We, on the other hand, carried out the analysis by using the combined image. This allows us to probe large and small scale structures simultaneously. In our analysis, the $N_{\rm HI}$ increases toward the head of the cloud and decreases afterward. The cold component shows the same $N_{\rm HI}$ pattern except that it peaks at a slightly different position from the warm component. There is a small velocity gradient at the tail of the cloud. Otherwise, velocity is constant for both cold and warm components.

The analysis of the combined image of HVC 310.3+08.1+167 was carried out on a smoothed cube due to it being very diffuse and low in surface brightness. It consists of many clumps, and all of them are unresolved with cold components. Overall, the velocity linewidth of both the cold and warm component follows the same trend as the $N_{\rm HI}$.

We discussed the HVC phase diagram (log P/k vs log n) using the model of Wolfire et al. (1995). The model has metallicity and gas-to-dust ratio of 0.3, which is based on the assumption that the gas was stripped from the LMC. All the clouds are in the instability valley where they can maintain their two-phase structures. Interestingly, there is an offset between the data points and their corresponding height above the Galactic plane. A lower metallicity model is a better fit for the majority of the data points, which suggests that the gas was likely stripped from the SMC. This is consistent with various simulations (e.g. Diaz & Bekki 2011). We find a gradient in thermal halo pressure, hydrogen density and H I column density as a function of Galactic latitude. This is the first possible observational evidence of an increasing Galactocentric distance from the trailing end to the leading part of the LA, although further observations may be needed to confirm. A different halo environment might explain the low star formation rate in the LA region. Special conditions such as additional dust and atomic hydrogen gas are needed in order to trigger star formation. Future studies of the atomic hydrogen gas content in the region and the search for more stars will be important to understand the star formation history in the region of the LA.

ACKNOWLEDGMENTS

B.-Q. F. was the recipient of a John Stocker Postdoctoral Fellowship from the Science and Industry Research Fund. N. Mc-G acknowledges CSIRO Astronomy & Space Science where this work was commenced. This publication made use of data products from the Parkes and ATCA radio telescopes. The Australia Telescope Compact Array/Parkes radio telescope is part of the Australia Telescope National Facility, which is funded by the Commonwealth of Australia for operation as a National Facility managed by CSIRO.

REFERENCES

Bechtol K., et al., 2015, ApJ, 807, 50
Ben Bekhti N., Brüns C., Kerp J., Westmeier T., 2006, A&A, 457, 917
Blitz L., Spergel D. N., Teuben P. J., Hartmann D., Burton W. B., 1999, ApJ, 514, 818
Braun R., Burton W. B., 1999, A&A, 341, 437
Brüns C., Westmeier T., 2004, A&A, 426, L9
Brüns C., Kerp J., Kalberla P. M. W., Mebold U., 2000, A&A, 357, 120
Brüns C., Kerp J., Pagels A., 2001, A&A, 370, L26
Brüns C., et al., 2005, A&A, 432, 45
Casetti-Dinescu D. I., Moni Bidin C., Girard T. M., Méndez R. A., Vieira K., Korchagin V. I., van Altena W. F., 2014, ApJL, 784, L37
Diaz J., Bekki K., 2011, MNRAS, 413, 2015
Drlica-Wagner A., et al., 2015, ApJ, 813, 109
For B.-Q., Staveley-Smith L., McClure-Griffiths N. M., 2013, ApJ, 764, 74
For B.-Q., Staveley-Smith L., Matthews D., McClure-Griffiths N. M., 2014, ApJ, 792, 43
Guhathakurta P., Reitzel D. B., 1998, in Zaritsky D., ed., Astronomical Society of the Pacific Conference Series Vol. 136, Galactic Halos. p. 22
Hartmann D., Burton W. B., 1997, Atlas of Galactic Neutral Hydrogen (Cambridge University Press)
Kalberla P. M. W., et al., 2010, A&A, 521, A17
Kenney J. D. P., van Gorkom J. H., Vollmer B., 2004, AJ, 127, 3361
Klypin A., Kravtsov A. V., Valenzuela O., Prada F., 1999, ApJ, 522, 82
Koposov S. E., Belokurov V., Torrealba G., Evans N. W., 2015, ApJ, 805, 130
Koribalski B. S., López-Sánchez Á. R., 2009, MNRAS, 400, 1749
Mathewson D. S., Cleary M. N., Murray J. D., 1974, ApJ, 190, 291
Matthews D., Staveley-Smith L., Dyson P., Muller E., 2009, ApJL, 691, L115
McClure-Griffiths N. M., et al., 2008, ApJL, 673, L143
McClure-Griffiths N. M., et al., 2009, ApJS, 181, 398
Moore B., Ghigna S., Governato F., Lake G., Quinn T., Stadel J., Tozzi P., 1999, ApJL, 524, L19
Muller C. A., Oort J. H., Raimond E., 1963, Academie des Sciences Paris Comptes Rendus, 257, 1661
Pietrzyński G., et al., 2013, Nature, 495, 76
Pisano D. J., Barnes D. G., Gibson B. K., Staveley-Smith L., Freeman K. C., Kilborn V. A., 2004, ApJL, 610, L17
Putman M. E., Saul D. R., Mets E., 2011, MNRAS, 418, 1575

Recillas-Cruz E., 1982, MNRAS, 201, 473
Salem M., Besla G., Bryan G., Putman M., van der Marel R. P., Tonnesen S., 2015, ApJ, 815, 77
Sault R. J., Teuben P. J., Wright M. C. H., 1995, in Shaw R. A., Payne H. E., Hayes J. J. E., eds, Astronomical Society of the Pacific Conference Series Vol. 77, Astronomical Data Analysis Software and Systems IV. p. 433 (arXiv:astro-ph/0612759)
Sembach K. R., Howk J. C., Savage B. D., Shull J. M., 2001, AJ, 121, 992
Stanimirović S., 2002, in Stanimirovic S., Altschuler D., Goldsmith P., Salter C., eds, Astronomical Society of the Pacific Conference Series Vol. 278, Single-Dish Radio Astronomy: Techniques and Applications. pp 375–396 (arXiv:astro-ph/0205329)
Stanimirović S., Hoffman S., Heiles C., Douglas K. A., Putman M., Peek J. E. G., 2008, ApJ, 680, 276
Steer D. G., Dewdney P. E., Ito M. R., 1984, A&A, 137, 159
Venzmer M. S., Kerp J., Kalberla P. M. W., 2012, A&A, 547, A12
Wakker B. P., 1991, A&A, 250, 499
Westmeier T., Brüns C., Kerp J., 2005, A&A, 432, 937
Westmeier T., Staveley-Smith L., Calabretta M., Jurek R., Koribalski B. S., Meyer M., Popping A., Wong O. I., 2015, MNRAS, 453, 338
Williams J. P., de Geus E. J., Blitz L., 1994, ApJ, 428, 693
Wilson W. E., et al., 2011, MNRAS, 416, 832
Wolfire M. G., McKee C. F., Hollenbach D., Tielens A. G. G. M., 1995, ApJ, 453, 673
Yozin C., Bekki K., 2015, MNRAS, 453, 2302
Zwaan M. A., 2001, MNRAS, 325, 1142